Progress In Electromagnetics Research B, Vol. 103, 139–157, 2023

Octa-Port High Gain MIMO Antenna Backed with EBG for mm-Wave Applications

Nallagundla Suresh Babu[1], Abdul Quaiyum Ansari[1], Sachin Kumar[2, *], Binod K. Kanaujia[3], Ghanshyam Singh[4], and Bhawna Goyal[5]

Abstract—This article presents a miniaturized octa-port high gain multiple-input-multiple-output (MIMO) antenna loaded with an electromagnetic band gap (EBG) layer for the use in 5G wireless communication applications. Each resonator of the presented antenna consists of a rectangular-like patch with truncated side edges and a partial ground plane. A layer of EBG unit cells is introduced underneath the antenna elements to increase the gain and restrain the surface wave effects, obtaining improved isolation amongst the resonating elements. The −10 dB impedance bandwidth of the prospective antenna with EBG is 12 GHz (21–33 GHz), and it provides isolation of $>$ 28 dB. The peak gain of the EBG-backed antenna is 17 dB. The presented mm-wave MIMO antenna offers decent diversity proficiency metrics like envelope correlation coefficient ($<$ 0.36), diversity gain ($\sim$ 10 dB), and total active reflection coefficient (−24.75 dB). The overall size of the octa-port MIMO antenna is 27.2 mm × 27.2 mm. The presented MIMO antenna could be used for n257/n258/n261 mm-wave bands.

1. INTRODUCTION

The increasing requirement for higher data throughput as well as constantly increasing carrier bandwidth has resulted in the advancement of wireless communication networks [1, 2]. Long-term evolution (LTE) and 4G standards are used by modern wireless systems to accommodate massive amounts of data and increasing bandwidth requirements [3, 4]. However, LTE/4G standards can only provide up to 20 Mbps of bandwidth, and mm-wave bands are required to achieve data speeds in Gbps [5, 6]. Article [7] provides an overview of the global allocation of 5G mm-wave spectrum, and most countries around the world are considering the 26/28 GHz range connectivity [8]. The mm-wave band offers increased data rates in Gbps, high throughput, low latency, and high-speed connectivity [9, 10]. However, the mm-wave range has some limitations, such as signal degradation and atmospheric absorptions [11]. They can be overcome by using multiple-input-multiple-output (MIMO) antennas, which increase channel capacity while providing high data rates and throughput [12]. However, compact MIMO antennas have the disadvantage of less separation distance between unit elements [13, 14], as it is difficult to arrange more radiating elements in a small area. Due to the close proximity, the interaction between radiators increases, degrading the overall working of the MIMO system. Thus, reducing inter-element coupling without significantly increasing the measurements/size of MIMO antenna is challenging. Compared with dual-port and quad-port MIMO antennas, designing a compact-size eight-port MIMO antenna is more difficult as the antenna elements must resist higher levels of mutual coupling [15].

Received 23 August 2023, Accepted 29 October 2023, Scheduled 10 November 2023
* Corresponding author: Sachin Kumar (gupta.sachin0708@gmail.com).
[1] Department of Electrical Engineering, Faculty of Engineering and Technology, Jamia Millia Islamia, New Delhi 110025, India. [2] Department of Electronics and Communication Engineering, SRM Institute of Science and Technology, Kattankulathur, Tamil Nadu 603203, India. [3] School of Computational and Integrative Sciences, Jawaharlal Nehru University, New Delhi 110067, India. [4] Department of Electronics and Communication Engineering, Feroze Gandhi Institute of Engineering and Technology, Reabareli 229316, India. [5] University Centre for Research and Development, Chandigarh University, Gharuan, Mohali, Punjab 140413, India.

In previous years, numerous strategies for reducing mutual coupling in two, four, and eight antenna elements have been presented. A defected ground plane with a zig-zag slot was presented in [16] to decrease mutual coupling in a four-element mm-wave MIMO antenna. The reported antenna had a complex design, only resonating at one frequency, large dimensions, and a low gain. A two-element mm-wave MIMO antenna with metasurface corrugation on the substrate edge to reduce mutual coupling was proposed in [17]. In [18], rectangular-shaped metal strips on the upper face of the dielectric resonators were introduced between mm-wave antenna elements. A metasurface array with unit cells in a circular split ring form was introduced among four radiators of the MIMO antenna in [19] for decreasing inter-element coupling. The antennas proposed in [17–19] were large in size, only resonating at one frequency, had low radiation efficiency and a low gain. In [20], two metallic vias were inserted into rectangle-shaped dielectric resonator antenna elements to decrease the coupling in a dual-element mm-wave MIMO antenna. In [21], rectangular semi-circle-shaped slots that act as metamaterial were loaded on the top surface of four rectangular dielectric resonator elements in an mm-wave four-element MIMO antenna. In [22], frequency selective surface (FSS) was used to decrease inter-element coupling in a four-port mm-wave MIMO antenna. In [23], a metamaterial-based structure was added between two resonators of a dielectric resonator antenna to decrease mutual coupling. In [24], an EBG array was introduced in a two-element 5G MIMO antenna to reduce mutual coupling. In [25], a four-element mm-wave 5G MIMO antenna was reported with a metasurface made up of periodic square-shaped patches for mutual coupling reduction. An eight-port MIMO antenna made of cylindrical-shaped dielectric resonator elements was presented in [26]. In [27], a four-element MIMO antenna with an edge-truncated slot and a superstrate to improve isolation was reported. However, the antennas in [20–27] used metallic vias and superstrates, which complicated fabrication, had a low peak gain value, resonating at only one resonating frequency, and low inter-element isolation.

This study presents a small octa-element high gain MIMO antenna with EBG for mm-wave applications. The antenna element is composed of a rectangle-shaped patch with truncated side edges and a partial ground plane. The MIMO antenna has eight identical rectangular-shaped resonators, with an EBG layer incorporated underneath the antenna to suppress surface wave effect and reduce inter-element coupling. The antenna functions in the frequency range of 21 to 33 GHz, covering the commonly used mm-wave 5G bands. The suggested eight-port antenna is simple to design and does not require any additional complex circuits to improve isolation. This article is ordered in the following manner. Section 2 discusses the design and analysis of single resonating element and octa-port MIMO antenna with and without EBG. Sections 3 and 4 present the results and conclusion, respectively.

2. ANTENNA DESIGN

The proposed octa-element mm-wave MIMO antenna is displayed in Fig. 1. The antenna is developed on an inexpensive FR-4 substrate material (thickness = 1.6 mm, dielectric constant = 4.4, and loss

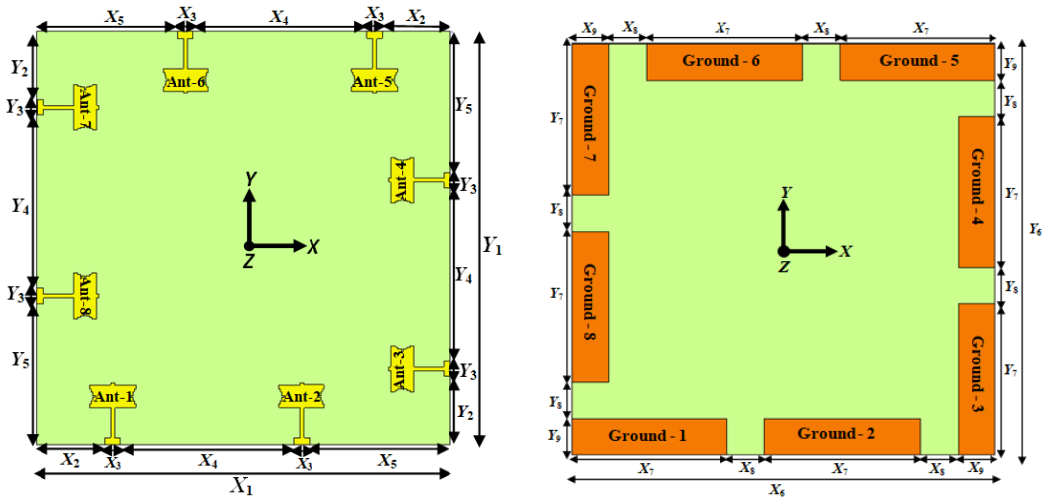

(a) (b)

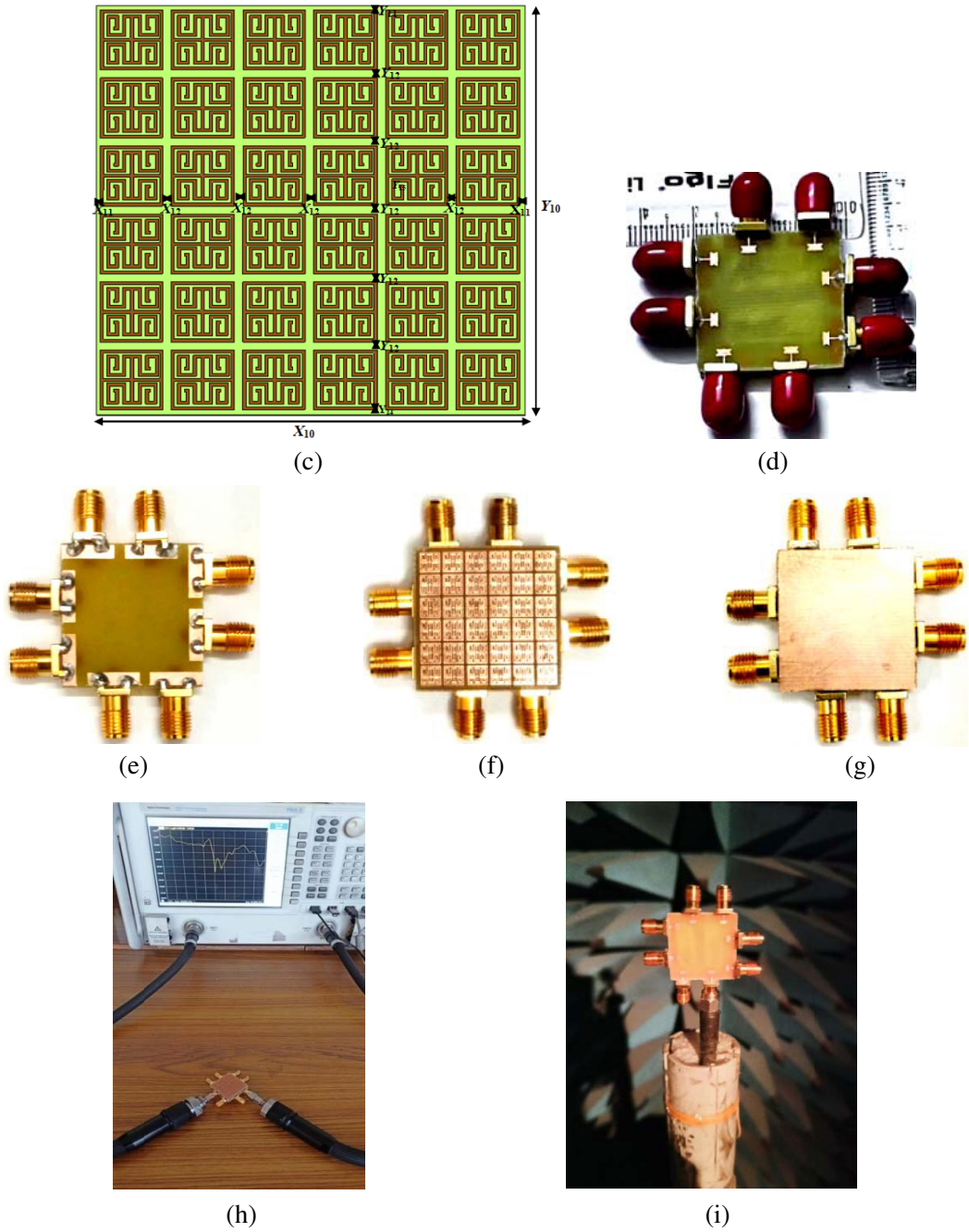

Figure 1. Octa-port MIMO antenna: (a) top view, (b) ground plane, (c) EBG array, (d) top view of fabricated prototype, (e) ground plane of fabricated prototype, (f) fabricated prototype with EBG array, (g) fabricated prototype with EBG ground plane, (h) S-parameter measurement, (i) far-field measurement in an anechoic chamber.

tangent = 0.02) using ANSYS HFSS high-frequency software. The orthogonal orientation of pairs of antenna elements increases the value of inter-element isolation. The total size of the octa-element mm-wave MIMO antenna with a 6×6 array of EBG unit cells is $27.2\,\text{mm}\times27.2\,\text{mm}$. The design specifications of the antenna are displayed in Table 1.

The development stages for the antenna element, and the EBG unit cell, are depicted in the following subsections.

Table 1. Design variables of octa-port mm-wave MIMO antenna (in mm).

Variable	Dimensions	Variable	Dimensions	Variable	Dimensions
W_1	5	L_9	0.1	X_6	27.2
L_1	10	W_9	0.29	Y_6	27.2
W_2	0.48	L_{10}	10	X_7	10
L_2	4.5	W_{10}	2.4	Y_7	10
W_3	1.97	W_{11}	5	X_8	2.4
L_3	1	X_1	27.2	Y_8	2.4
L_4	0.375	Y_1	27.2	X_9	2.4
W_5	3.6	X_2	4.5	Y_9	X_8
L_5	0.25	Y_2	4.5	X_{10}	27.2
L_6	3	X_3	1	Y_{10}	27.2
W_6	0.1	Y_3	1	X_{11}	0.1
L_7	0.2	X_4	11.4	Y_{11}	0.1
W_7	0.25	Y_4	11.4	X_{12}	0.2
L_8	0.075	X_5	9.3	Y_{12}	0.2
W_8	0.16	Y_5	9.3		

2.1. Development of Antenna Element

Figure 2 displays the architecture of mm-wave antenna element. Design specifications of the antenna are detailed in Table 1. Fig. 3 depicts the development stages of a single radiator. In the first step, a common rectangle-shaped patch (antenna 1) and a partial ground surface are considered, as shown in Fig. 3(a). Antenna 1 has a physical size of $(L_1 \times W_1)$ and is tuned to 28 GHz. The dimension of the rectangular patch at the resonant frequency of 28 GHz is calculated using Equation (1).

$$L_6 = \frac{c}{2f_r\sqrt{\varepsilon_{eff}}} \tag{1}$$

$$\varepsilon_{eff} = \frac{\varepsilon_r + 1}{2} \tag{2}$$

The resonant frequency of the antenna is 28 GHz, with a resonating bandwidth of 1.4 GHz (27.4–28.8 GHz), as presented in Fig. 3(e).

In the second stage, slits with dimensions of $(L_7 \times W_6)$ are carved out from the centre of the two sides of the rectangular radiator, as illustrated in Fig. 3(b). By using the technique of carving slits [28], the length and width of the prospective antenna element change from (3 mm × 1.5 mm) to $(L_6 \times W_6 = 2.6\,\text{mm} \times 1.4\,\text{mm})$. Also, by curtailing the edges of length $(L_7) = 0.2$ mm and width $(W_6) = 0.1$ mm on both sides, the new resonant frequency at 27 GHz is obtained (using Equation (1)). The objective of rectangular slits is to enlarge the direction of current flow, which forces the resonant frequency to resonate at a lower frequency of 26 GHz with the improvement in bandwidth of 3.6 GHz (from 25.1–28.7 GHz).

In the third stage, slits with dimensions of $(L_8 \times W_7)$ are carved out of the centre of the two sides of the rectangular radiator, as illustrated in Fig. 3(c). Furthermore, by curtailing the edges of length $(L_8) = 0.075$ mm and width $(W_7) = 0.25$ mm on both sides, an increase in bandwidth of 4.7 GHz from (25–29.7 GHz), with a resonant frequency of 27.4 GHz, is achieved. In the final phase (Fig. 3(d)), another rectangular slit with dimensions of $(L_9 \times W_8)$ is carved out from both sides of antenna for better −10 dB impedance bandwidth of 8 GHz (from 23–31 GHz). The gain of the suggested antenna element is displayed in Fig. 3(f).

2.2. Design/Characterization of the EBG Unit Cell

EBG structures are synthetic periodic patterns that promote or inhibit the transmission of electromagnetic waves in the defined spectrum for all incident angles and modes of polarization [29].

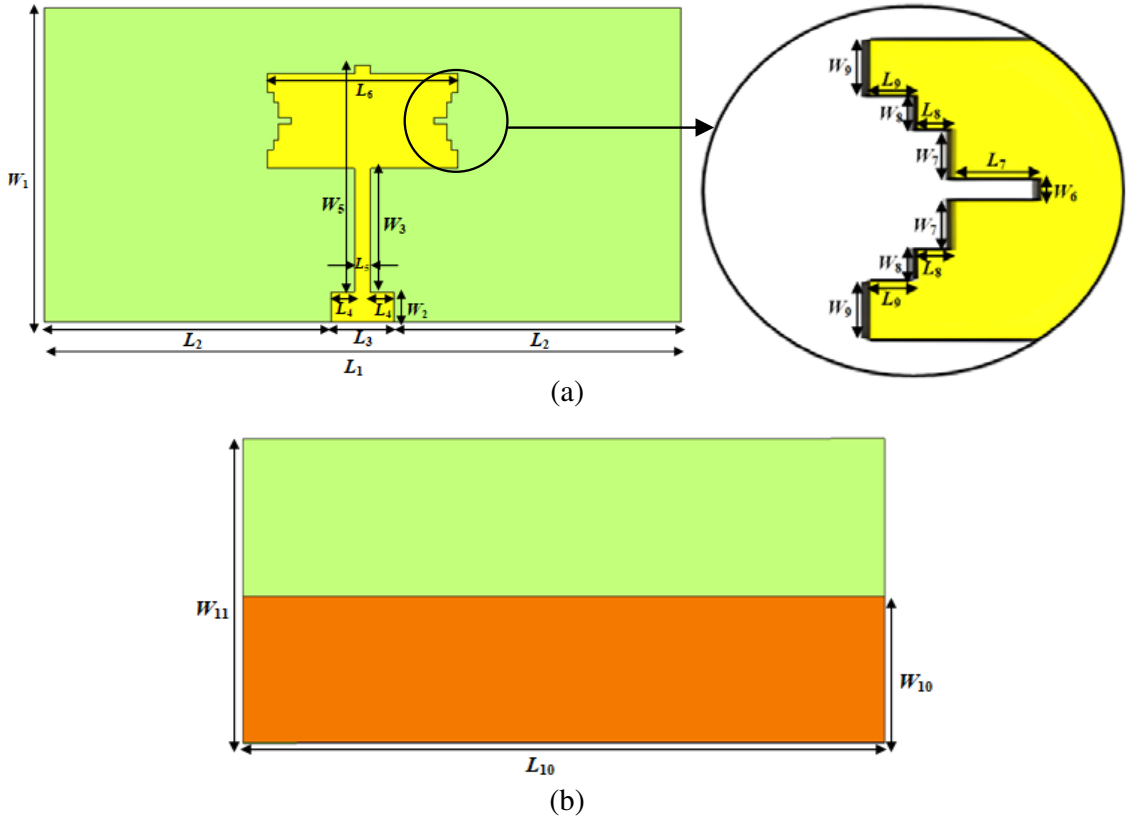

Figure 2. Architecture of the mm-wave unit element: (a) radiator, (b) ground plane.

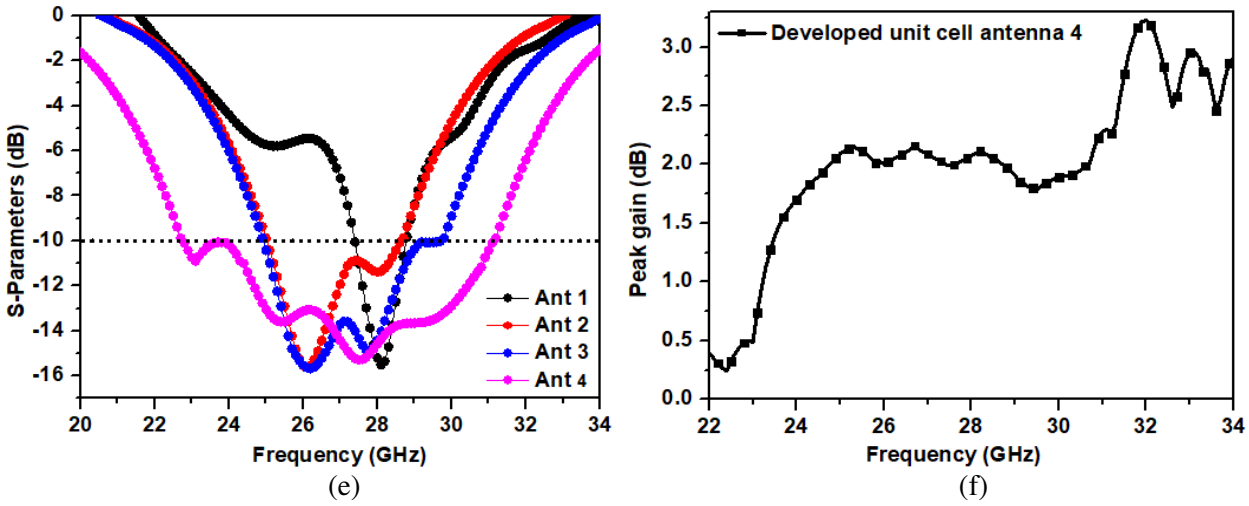

Figure 3. Development stages of the mm-wave antenna element: (a) antenna 1, (b) antenna 2, (c) antenna 3, (d) antenna 4, (e) S_{11} characteristics, (f) gain.

They are periodic arrangements made of metallic strip or slotted conducting or insulating materials. The attributes of the antenna can be modified by incorporating an EBG design on conductive materials. The primary advantage of EBG structures is their ability to reduce the effect of surface wave current. The surface wave decreases antenna gain and efficiency, increases cross-polarization and end-fire radiation, resulting in a poor antenna performance [30]. Surface waves also increase the coupling between neighbouring antenna elements in an antenna array. When the antenna is integrated with EBG, the surface-wave suppresses and improves the functionality of the antenna by increasing antenna gain and lowering backward radiations [31].

An EBG array with a mushroom-shaped element was reported in [32], which included a ground surface, dielectric substrate material, metallic strip patches, and shorted vias. The EBG array exhibited stopband characteristics, which prevented surface-wave propagation. The operation of the EBG structure was described using an LC equivalent circuit, which acts as an electrical stopband filter to prevent surface wave propagation [33]. The flow of current through the shorted vias produces the inductor L, and the gap between the adjacent patches produces the capacitor C. The inductor and capacitor values for an EBG structure with patch width (W), gap width (g), substrate thickness (h), and dielectric constant (ε_r) are calculated using the following equations [34].

$$L = \mu_0 h \tag{3}$$

$$C = \frac{W\varepsilon_0(1+\varepsilon_0)}{\pi}\cosh\frac{(2W+g)}{g} \tag{4}$$

In free space condition, the permeability (μ_0) and permittivity (ε_0) are given as,

$$\omega = \frac{1}{\sqrt{LC}} \tag{5}$$

$$BW = \frac{\Delta\omega}{\omega} = \frac{1}{\eta}\sqrt{\frac{L}{C}} \tag{6}$$

The EBG array presented in this article is used to enhance the features of the presented mm-wave antenna. The suggested EBG unit cell is displayed in Fig. 4(a), and its equivalent circuit model is illustrated in Fig. 4(b). The EBG is made up of a square-shaped unit cell enclosing two pairs of spiral arms connected side by side on the upper side and a mirror image of the first pair of spiral arms on the bottom side. Table 2 shows the contribution of various inductors and capacitors used in the EBG unit cell element. The unit cell's metal strip is represented by inductance (L), and the space between them is represented by capacitance (C). The EBG unit cell element is also developed on cost-effective

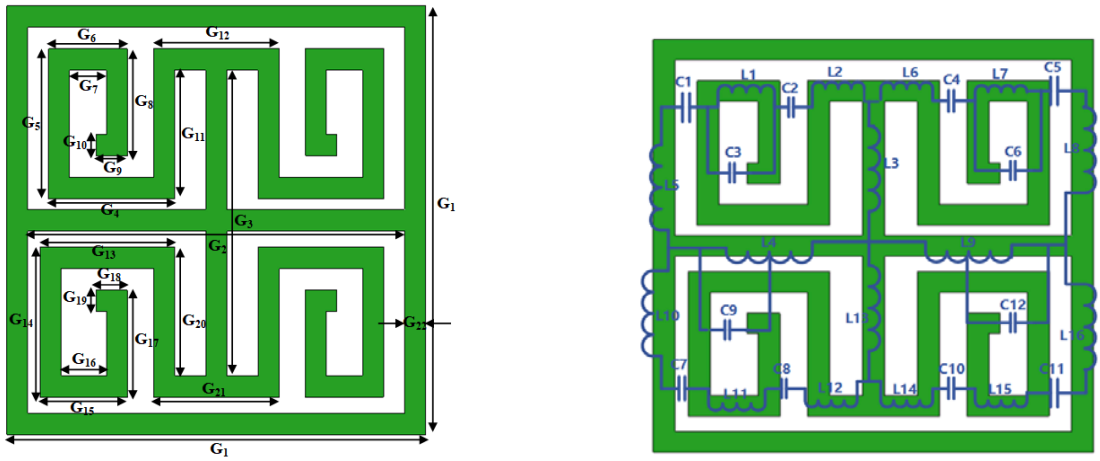

(a) (b)

Figure 4. Proposed EBG unit cell: (a) dimensions, (b) equivalent circuit model.

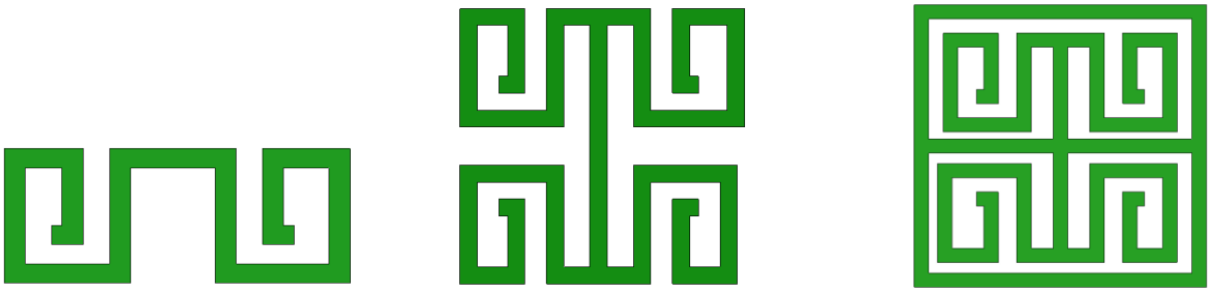

(a) (b) (c)

Figure 5. Evolution phases of EBG unit cell: (a) unit cell 1, (b) unit cell 2, (c) unit cell 3.

FR-4 epoxy material with the same specifications. The unit cell is developed (steps are shown in Fig. 5) by using ANSYS HFSS software, and its reflection phase characteristics are shown in Fig. 6. The measurements of EBG unit cell element are shown in Table 3.

Figure 5 depicts the development phases of the proposed EBG unit cell. Initially, a spiral coil is connected side by side to an identical coil, as displayed in Fig. 5(a). The reflection amplitude and phase of EBG unit cells 1, 2, and 3 are depicted in Figs. 6(a) and (b), respectively. The reflection amplitude of EBG unit cell 1 is -22 dB at 28 GHz at reflection phase of 0°. In Fig. 6(b), the surfaces at upper side (27 GHz) and lower side (29.5 GHz), with corresponding reflection phases of +180° and −180° (for EBG unit cell 1), act as a perfect electric conductor (PEC) [35]. Similarly, the surfaces at upper side (27.2 GHz) and lower side (29 GHz), with corresponding reflection phases of +90° and −90° behave like a perfect magnetic conductor (PMC). Hence, the obtained resonant frequency of EBG unit cell 1 is 28 GHz at the reflection phase of 0° with a bandwidth of 1.8 GHz. Then, on the upper side, a pair of spiral coils is introduced, with its mirror image on the bottom side. The two pairs are joined together by a rectangular strip, as shown in Fig. 5(b).

The EBG unit cell 2 has a resonant frequency of 26 GHz in coincidence with the resonant frequency of 28 GHz. The reflection amplitude of EBG unit cell 2 is -22.5 dB at 26 GHz at reflection phase of 0° as shown in Fig. 6(a). The surfaces at upper side (21 GHz) and lower side (27 GHz), with corresponding reflection phases of +180° and −180° (for EBG unit cell 2), act as a PEC. Similarly, the surfaces at upper side (23.5 GHz) and lower side (25.9 GHz), with corresponding reflection phases of +90° and −90°, behave like a PMC. Therefore, the obtained resonant frequency of EBG unit cell 2 is 26 GHz at the reflection phase of 0° with a bandwidth of 2.4 GHz. Furthermore, as shown in Fig. 5(c), a horizontal

Table 2. Strip contribution in terms of reactive element.

Reactive element	Metal strip/spacing between them	Location of strip/spacing	Connecting strip
L_1	Horizontal spiral arm	Upper left	—
L_2	Horizontal spiral arm connector	Upper left	Upper right and vertical strips
L_3	Vertical strip	Upper middle	Upper left and right strips
L_4	Horizontal strip	Left middle	Vertical upper and bottom left square EBG cell
L_5	Vertical strip	Upper left	Bottom left square EBG cell
L_6	Horizontal spiral arm connector	Upper right	Upper right and upper left
L_7	Horizontal spiral arm	Upper right	—
L_8	Vertical strip	Upper right	Bottom right square EBG cell
L_9	Horizontal strip	Right middle	Vertical upper and bottom right square EBG cell
L_{10}	Vertical strip	Bottom left	Upper left square EBG cell
L_{11}	Horizontal spiral arm	Bottom left	—
L_{12}	Horizontal spiral arm connector	Bottom left	Bottom right and vertical strips
L_{13}	Vertical strip	Bottom middle	Bottom left and right strips
L_{14}	Horizontal spiral arm connector	Bottom right	Bottom right and upper left
L_{15}	Horizontal spiral arm	Bottom right	—
L_{16}	Vertical strip	Bottom right	Upper left square EBG cell
C_1	Horizontal spacing	Spacing between upper left spiral arm and square EBG cell	—
C_2	Horizontal spacing	Spacing between upper left spiral arm and its connecting strip	—
C_3	Horizontal spacing	Spacing between one edge to another edge of upper left spiral arm	—
C_4	Horizontal spacing	Spacing between upper right spiral arm and its connecting strip	—
C_5	Horizontal spacing	Spacing between upper right spiral arm and square EBG cell	—
C_6	Horizontal spacing	Spacing between one edge to another edge of upper right spiral arm	—
C_7	Horizontal spacing	Spacing between bottom left spiral arm and square EBG cell	—
C_8	Horizontal spacing	Spacing between bottom left spiral arm and its connecting strip	—
C_9	Horizontal spacing	Spacing between one edge to another edge of bottom left spiral arm	—
C_{10}	Horizontal spacing	Spacing between bottom right spiral arm and its connecting strip	—
C_{11}	Horizontal spacing	Spacing between bottom right spiral arm and square EBG cell	—
C_{12}	Horizontal spacing	Spacing between one edge to another edge of bottom right spiral arm	—

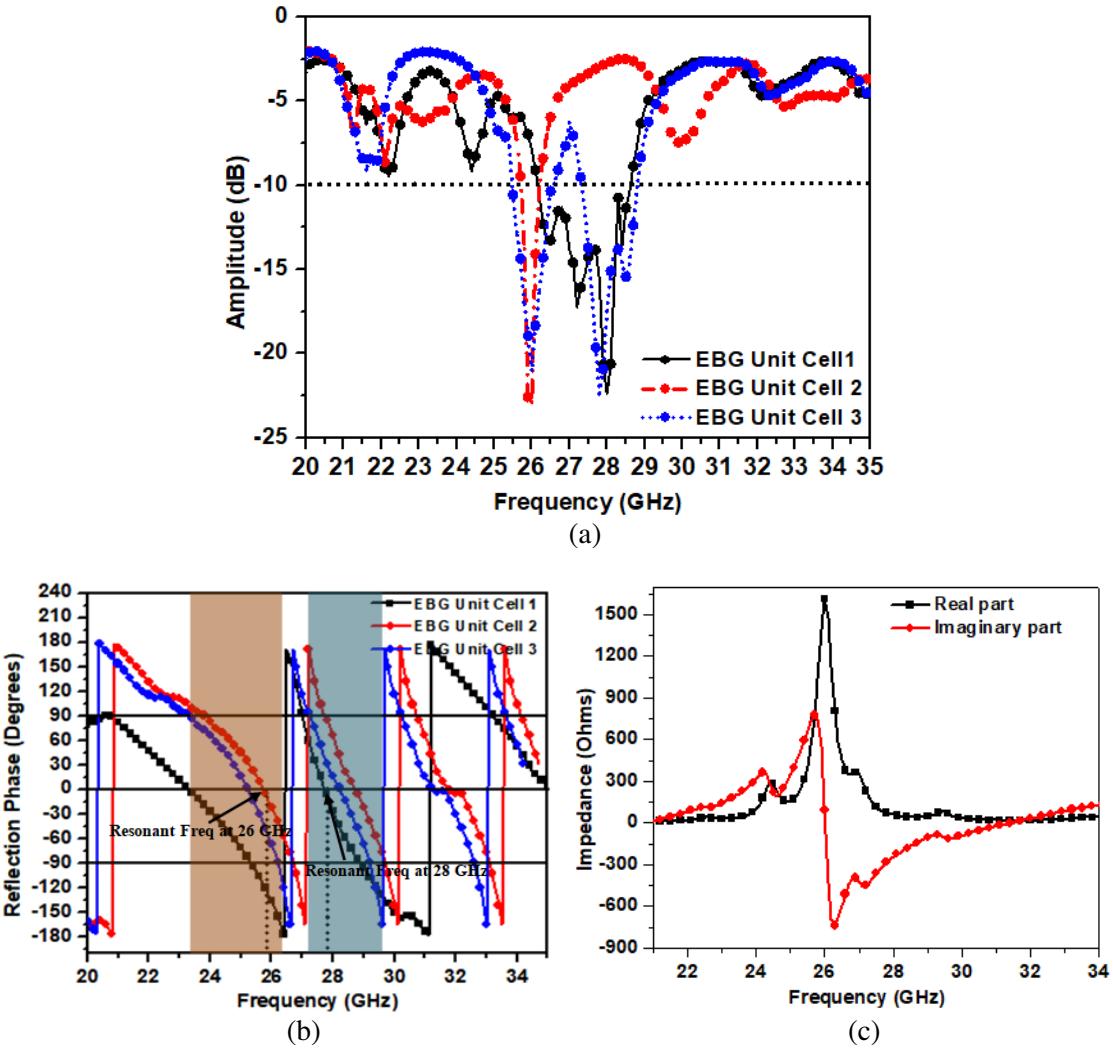

Figure 6. EBG unit cell attributes: (a) reflection amplitude, (b) reflection phase, (c) impedance.

Table 3. Design variables of EBG unit cell (in mm).

Variable	Dimensions	Variable	Dimensions	Variable	Dimensions
G_1	4	G_8	1	G_{15}	0.83
G_2	3.6	G_9	0.3	G_{16}	0.43
G_3	2.85	G_{10}	0.2	G_{17}	1
G_4	1.2	G_{11}	1.2	G_{18}	0.3
G_5	1.4	G_{12}	1.2	G_{19}	0.2
G_6	0.75	G_{13}	1.28	G_{20}, G_{21}	1.2
G_7	0.35	G_{14}	1.4	G_{22}	0.2

rectangular strip is introduced exactly between the centres of two pairs of spiral coils, which are encircled by a square-shaped metallic strip.

The EBG unit cell 3 is used to improve matching, resulting in resonating two different frequencies (at 28 GHz and 26 GHz) with increased bandwidth. The reflection amplitude of EBG unit cell 3 is -22 dB at

28 GHz and 26 GHz at reflection phase of 0° as shown in Fig. 6(a). The surfaces at upper side (26.8 GHz) and lower side (29.2 GHz), with corresponding reflection phases of +180° and −180°, act as a PEC. Similarly, the surfaces at upper side (20.2 GHz) and lower side (27.2 GHz), with corresponding reflection phases of +180° and −180°, behave like a PEC. Furthermore, the surfaces at upper side (27.2 GHz) and lower side (29 GHz), with corresponding reflection phases of +90° and −90° behave like a PMC. Therefore, the obtained resonant frequency of EBG unit cell 3 is 28 GHz at the reflection phase of 0° with a bandwidth of 1.8 GHz. Also, the surfaces at upper side (23.3 GHz) and lower side (26.4 GHz), with corresponding reflection phases of +90° and −90°, behave like a PMC, and the obtained resonant frequency of EBG unit cell 3 is 26 GHz at the reflection phase of 0° with a bandwidth of 3.1 GHz.

The impedance characteristic curve of the proposed EBG unit cell (Fig. 4(b)) is analysed using the HFSS tool. It shows simulated results for the real and imaginary impedance components at the desired frequency of 26 GHz, as shown in Fig. 6(c). The component values of inductances and capacitances used in the EBG unit cell configuration are calculated using the Keysight ADS tool [36] and listed in Table 4. The resonant frequency of the unit cell is calculated as,

$$f_r = \frac{1}{2\pi\sqrt{L_{eq}C_{eq}}} \tag{7}$$

where $L_{eq} = 0.25\,\text{nH}$, which is the summation of all inductances from L_1 to L_{16}, and $C_{eq} = 0.15\,\text{pF}$, which is the summation of all capacitances from C_1 to C_{12}.

Table 4. Component values of the proposed EBG unit cell (all inductances are in nH and all capacitances are in pF).

Component	Value	Component	Value	Component	Value
L_1	0.019	L_6	0.017	L_{11}	0.019
C_1	0.0127	C_6	0.0123	C_{11}	0.0127
L_2	0.017	L_7	0.019	L_{12}	0.017
C_2	0.0125	C_7	0.0127	C_{12}	0.0123
L_3	0.015	L_8	0.013	L_{13}	0.015
C_3	0.0123	C_8	0.0125	L_{14}	0.017
L_4	0.013	L_9	0.013	L_{15}	0.019
C_4	0.0125	C_9	0.0123	L_{16}	0.013
L_5	0.013	L_{10}	0.013		
C_5	0.0127	C_{10}	0.0125		

By substituting the obtained values listed in Table 4 in Equation (7), the resonant frequency is evaluated as,

$$f_r = \frac{1}{2\pi\sqrt{\left(0.15\times10^{-12}\right)\left(0.25\times10^{-9}\right)}} = 26\,\text{GHz}$$

Hence, the simulated results are validated with the theoretical values of EBG unit cell configuration.

3. RESULTS AND DISCUSSION

3.1. Reflection Coefficients

The manufactured prototype of octa-element mm-wave MIMO antenna with its measurement in an anechoic chamber is demonstrated in Figs. 1(e)–(i). Fig. 7 depicts the simulated/experimental impedance bandwidth of the mm-wave octa-element MIMO antenna. The experimental −10 dB impedance bandwidth of octa-element MIMO antenna is 8.4 GHz (22.8–31.2 GHz) without EBG. Without EBG, the simulated bandwidth is 9 GHz (22.5–31.5 GHz), whereas with EBG, it is 12 GHz (21–33 GHz).

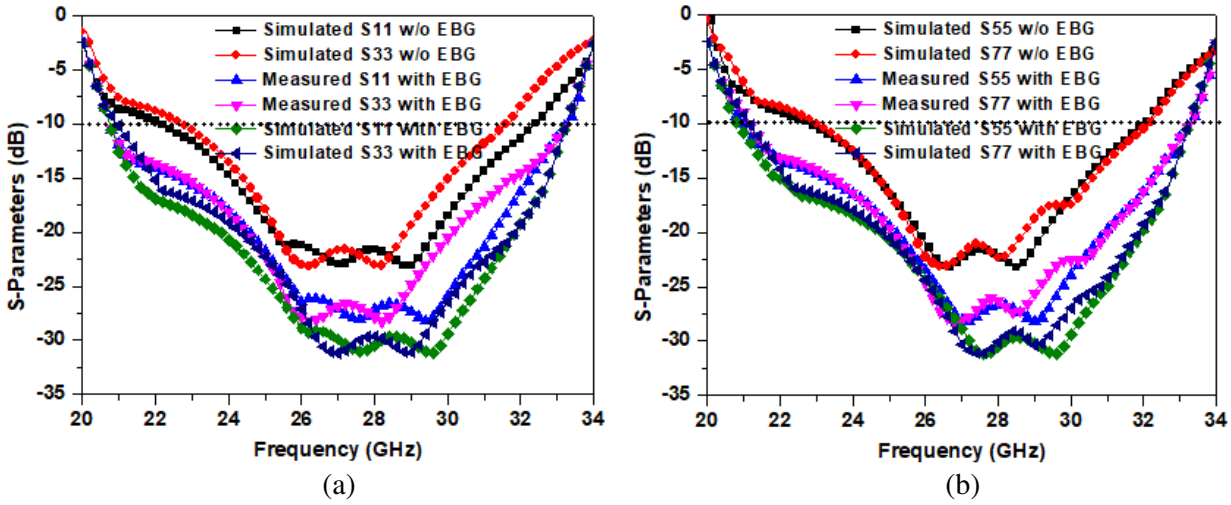

Figure 7. S-parameters of the octa-element mm-wave MIMO antenna with and without EBG: (a) S_{11} and S_{33}, (b) S_{55} and S_{77}.

3.2. Mutual Coupling

Figure 8 depicts the S-parameters of the mm-wave octa-element MIMO antenna. Without EBG, the isolation between resonating elements is more than 18 dB and more than 28 dB when EBG is used in the operating bandwidth.

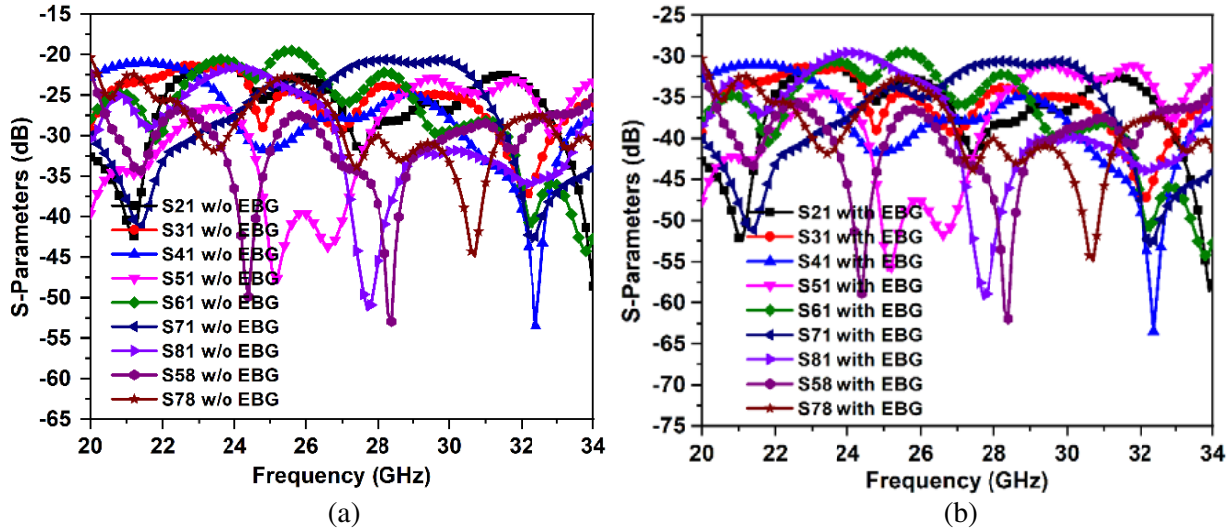

Figure 8. S-parameters of the octa-element mm-wave MIMO antenna: (a) without EBG, (b) with EBG.

3.3. Gain

The simulated/measured gain values of the mm-wave 5G MIMO antenna having eight elements are displayed in Fig. 9. The simulated peak gain with EBG is 18 dB, while the measured peak gain with EBG is 17 dB. The simulated peak gain without EBG is 10 dB, and the measured peak gain without EBG is 9 dB.

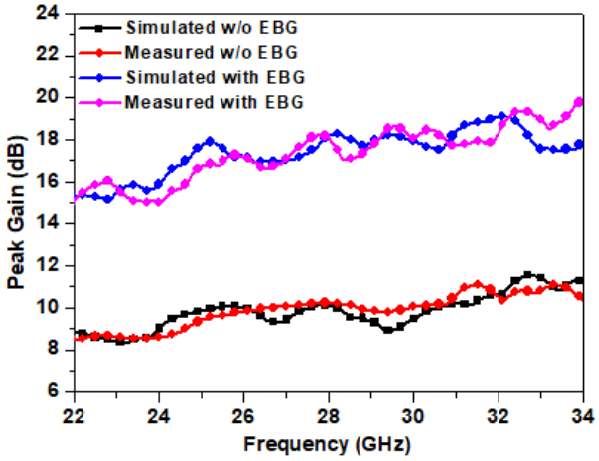

Figure 9. Gain of the octa-element mm-wave MIMO antenna with and without EBG.

3.4. MIMO/Diversity Antenna Performance

3.4.1. ECC

The calculation of envelope correlation coefficient (ECC) is critical for determining how each component of the MIMO system is uncorrelated from the others. The ECC between neighbouring antenna elements 1 and 2 can be calculated using the relation [37].

$$\rho_e = \frac{\left| \iint \left[\vec{F}_1(\theta,\varphi)\, \vec{F}_2(\theta,\varphi) \right] d\Omega \right|^2}{\iint \left| \vec{F}_1(\theta,\varphi) \right|^2 d\Omega \iint \left| \vec{F}_2(\theta,\varphi) \right|^2 d\Omega} \tag{8}$$

The obtained ECC values for the proposed mm-wave octa-element MIMO antenna are displayed in Figs. 10(a) and (b). According to the curves, the simulated ECC without EBG is 0.36, whereas the simulated value of ECC with EBG is 0.30, and the measured ECC with EBG is 0.29.

3.4.2. Diversity Gain

Diversity gain (DG) is an essential factor in MIMO antenna design. It shows how much any diversity method reduces transmitted power. The ECC may be used to determine DG for a MIMO antenna configuration [38].

$$DG = 10\sqrt{(1 - ECC^2)} \tag{9}$$

Figure 10(c) displays the simulated and experimental DGs with and without EBG. The measured DG without EBG is 9.98 dB, while the simulated DG without EBG is 9.96 dB. Similarly, the simulated DG with EBG is 9.99 dB, while the measured DG with EBG is nearly equal to 10 dB.

3.4.3. Total Active Reflection Coefficient (TARC)

Total active reflection coefficient (TARC) refers to the overall return loss of the MIMO antenna elements. It is introduced as a parameter used to characterize the bandwidth and efficiency of a MIMO system. It is calculated using the S-parameters and reflection coefficients between various elements of the MIMO antenna system. It shows how the TARC curves varies with different phase combinations, and phase information is crucial in MIMO systems as it can significantly affect the system performance. S-parameters are used to calculate TARC of the proposed eight-element MIMO antenna. It is computed

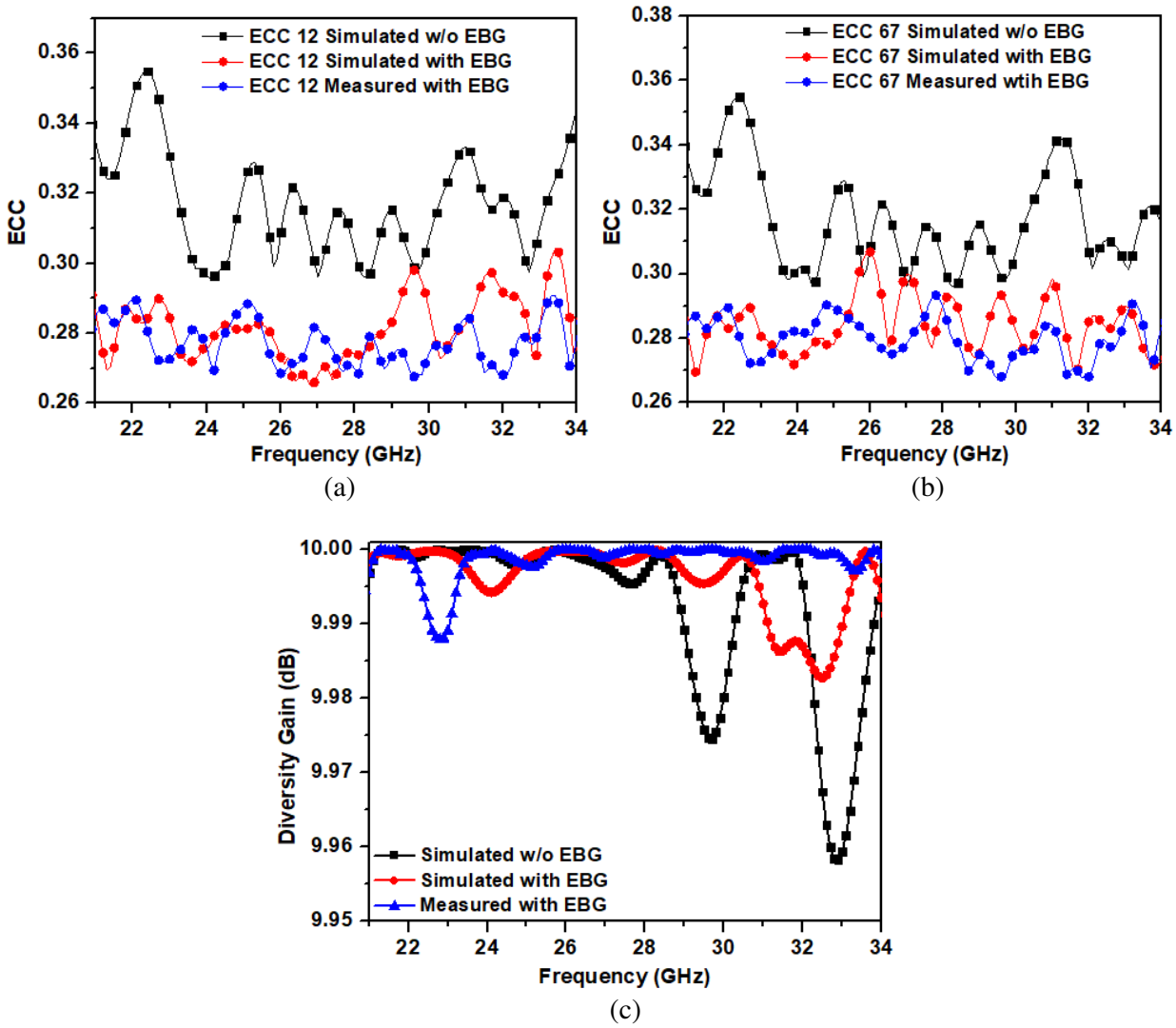

Figure 10. Performance behaviour of octa-element mm-wave MIMO antenna: (a) ECC 12 with and without EBG, (b) ECC 67 with and without EBG, (c) DG with and without EBG.

using dispersion characteristics of two antennas by using the following equation [39].

$$TARC = \sqrt{\frac{|S_{11} + S_{22}e^{j\vartheta}|^2 + |S_{21} + S_{22}e^{j\vartheta}|^2}{2}} \tag{10}$$

Figure 11 illustrates the graphical representation of the simulated/experimental TARC values of the presented antenna for different phase combinations from 0° to 180°. The simulated value of TARC at 28 GHz is −28 dB, whereas the experimental value is −27 dB.

3.5. Surface Current Distribution

The surface current distributions of the suggested octa-port mm-wave MIMO antenna at 25 GHz, 26 GHz, 27 GHz, and 28 GHz are illustrated in Fig. 12. The density of surface current from antenna element 1 to elements 2, 3, 4, 5, 6, 7, and 8 is very weak, which is due to the presence of the EBG layer. Therefore, the proposed antenna results in improved isolation.

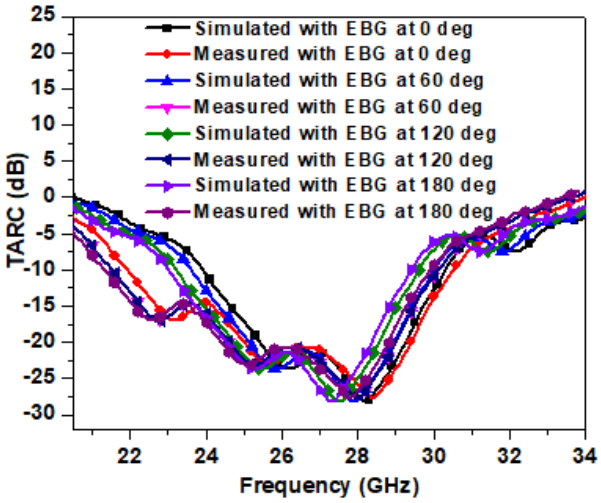

Figure 11. TARC curves of the proposed octa-element mm-wave MIMO antenna.

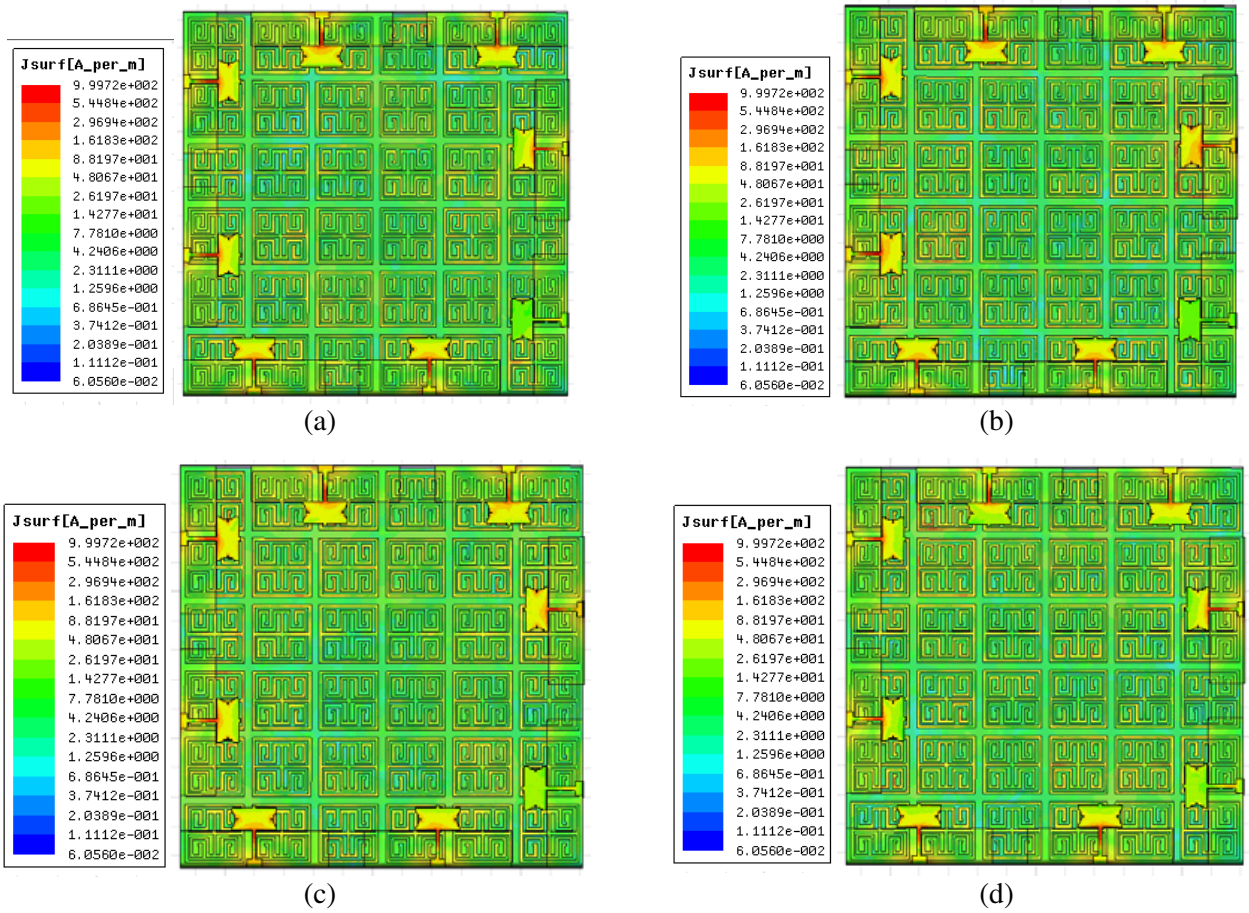

Figure 12. Surface current distributions of the octa-port mm-wave MIMO antenna: (a) 25 GHz, (b) 26 GHz, (c) 27 GHz, (d) 28 GHz.

3.6. Radiation Pattern

Figure 13 depicts the radiation characteristics of mm-wave octa-element MIMO antenna at 26 GHz and 28 GHz for the first, second, fourth, and eighth ports. The patterns are determined with one

port resonating and other ports matched through a terminator of 50 Ω. It is found that all resonating elements exhibit almost omnidirectional behaviour.

In Table 5, the presented octa-element antenna is compared to other published mm-wave MIMO antennas. The prospective antenna has a smaller size, wider bandwidth, higher isolation, higher peak gain, lower DG value, and a higher ECC value than the reported antennas.

The following are the primary benefits of the suggested antenna:

- The EBG-based octa-port mm-wave (26 GHz/28 GHz) MIMO antenna with dimensions of 27.2 mm × 27.2 mm is rarely reported in the literature.
- Unlike previously reported mm-wave 5G MIMO antenna designs, the presented antenna covers the frequencies 26.5–29.5 GHz (n257), 24.25–27.5 GHz (n258), and 27.5–28.35 GHz (n261).
- Unlike previously reported antenna configurations that used complicated patch [16] and vias [20],

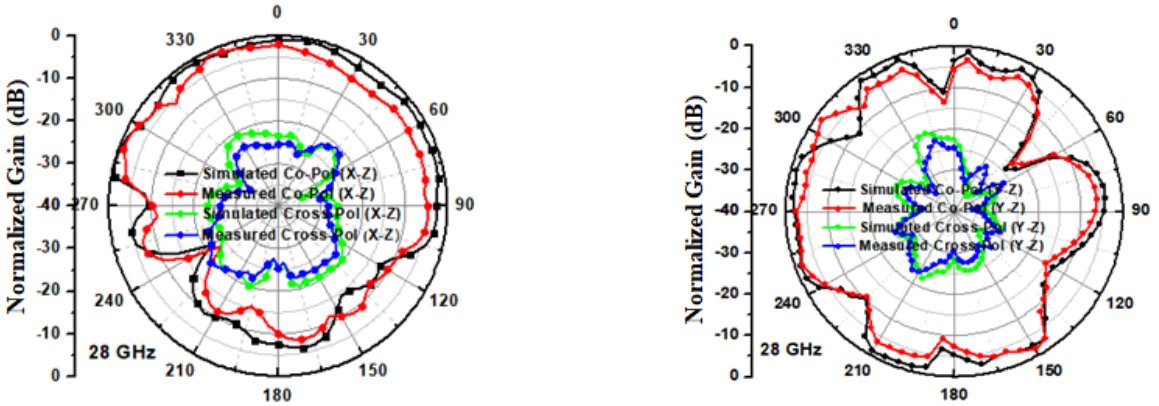

(a)

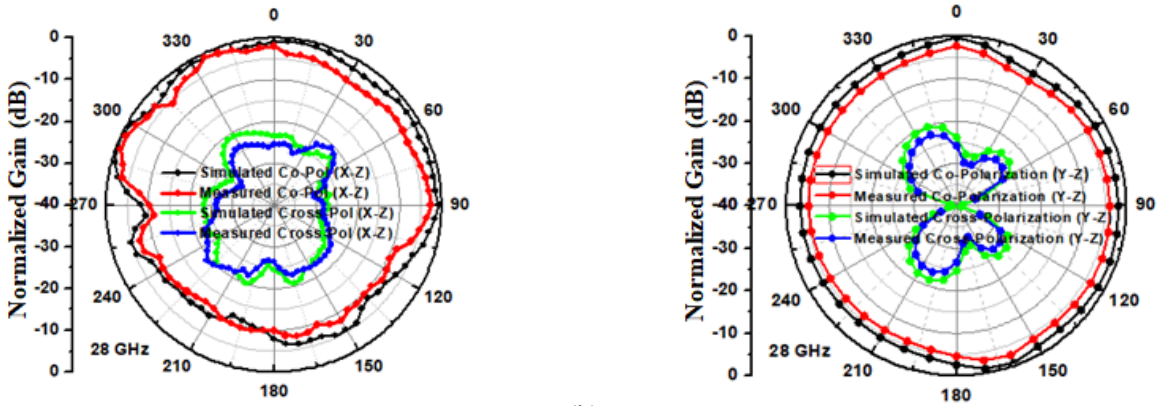

(b)

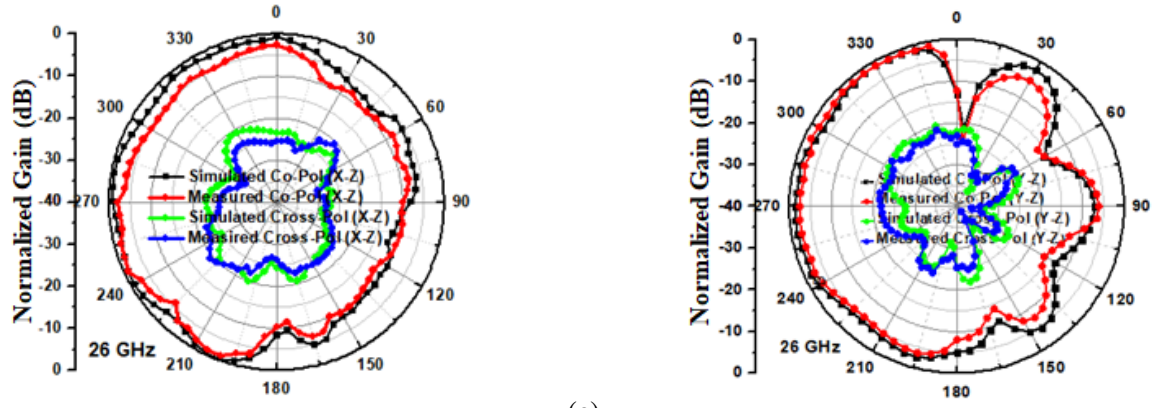

(c)

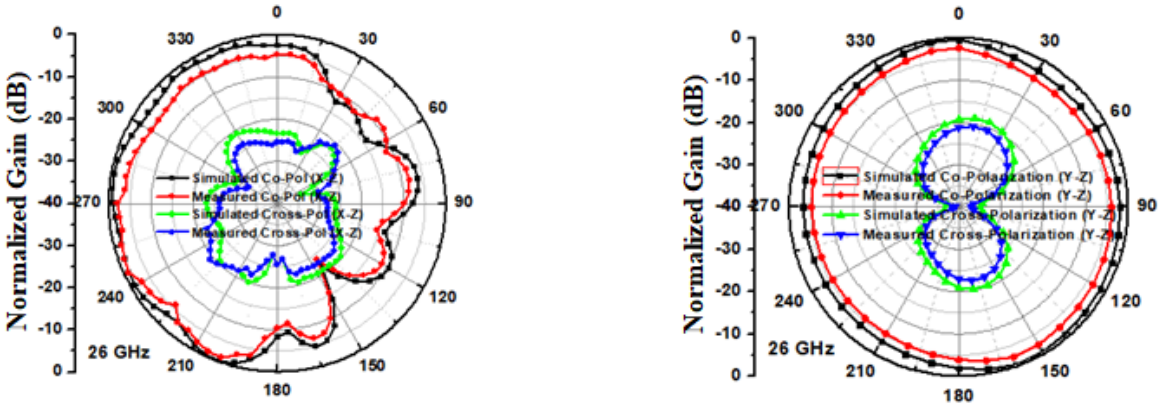

(d)

Figure 13. Radiation behaviour of the proposed mm-wave octa-port MIMO antenna: (a) port 1 at 28 GHz, (b) port 2 at 28 GHz, (c) port 4 at 26 GHz, (d) port 8 at 26 GHz.

Table 5. Proposed octa-port MIMO antenna compared with other published mm-wave MIMO antennas.

Ref.	Dimensions ($L \times W$)	No. of ports	Structure Type	Operating band (GHz)	−10 dB bandwidth (GHz)	Isolation (dB)	Peak gain (dB)	DG (dB)	ECC	TARC (dB)
[16]	$2.55\lambda_0 \times 3.45\lambda_0$	4	Double-layered	25.5–29.6	4.1	> 15	8.3	9.9	< 0.01	—
[17]	$7.65\lambda_0 \times 1.89\lambda_0$	2	Single-layered	27–32	5	—	17.9	—	—	—
[18]	$1.82\lambda_0 \times 1.82\lambda_0$	2	Double-layered	27.25–28.59	1.34	> 24	—	9.9	< 0.013	−25
[19]	$2.45\lambda_0 \times 3.52\lambda_0$	4	Double-layered	24.55–26.5	1.95	> 45	10.3	9.9	< 0.1	—
[20]	$1.82\lambda_0 \times 0.92\lambda_0$	2	Double-layered	25.1–27	1.9	> 34	6.4	—	—	—
[21]	$1.78\lambda_0 \times 3.56\lambda_0$	4	Double-layered	26.71–28.91	2.2	> 29	7.5	9.9	< 0.05	—
[22]	$2.52\lambda_0 \times 2.52\lambda_0$	4	Double-layered	28–33	5	> 25	—	—	—	—
[23]	—	2	Double-layered	57–64	7	> 22	—	—	< 0.1	—
[24]	$2.61\lambda_0 \times 2.61\lambda_0$	2	Double-layered	23–25	2	> 37	6	9.7	< 0.24	—
[25]	$1.70\lambda_0 \times 1.70\lambda_0$	4	Multi-layered	25–31	6	> 30	11	9.9	< 0.015	—
[26]	$4.76\lambda_0 \times 2.08\lambda_0$	8	Multi-layered	29.75–31.5	1.75	> 25	8	9.9	< 0.002	—
[27]	$1.58\lambda_0 \times 1.58\lambda_0$	4	Double-layered	25–33	8	—	14	—	< 0.008	—
Prop.	$1.90\lambda_0 \times 1.90\lambda_0$	8	Double-layered	21–34	13	> 28	17	9.9	< 0.36	−27.5

the proposed antenna uses slot, slit, and stub.

- The proposed antenna design is simple to fabricate and improves isolation without requiring any additional active elements because of the orthogonal orientation of resonating elements and the EBG layer.
- The proposed antenna uses less substrate area than previously reported mm-wave MIMO antennas [16, 17, 19, 21, 22, 24, 26] while providing wider bandwidth and high gain.
- The presented antenna has an improved DG of ∼ 10 dB, which provides benefits such as better signal quality, increased data throughput, extended coverage, better resistance to interference, support for multiple users, and remarkable adaptability to variable environmental conditions.
- In addition to mm-wave 5G applications, the presented antenna can be used for body wearable applications covering 24.05–24.25 GHz band [40].
- The incorporation of an EBG configuration within the MIMO antenna effectively mitigates surface wave interference, resulting in a substantial improvement in the isolation between the resonating elements.

4. CONCLUSION

An EBG-based miniaturized octa-element MIMO antenna for mm-wave 5G applications is suggested in this paper. The antenna element is composed of a partial ground plane, a rectangular-shaped patch slotted at both edges, and a microstrip feed line. The MIMO antenna consists of eight identical elements that are arranged orthogonal to each other in order to attain high isolation. The EBG array introduced in the MIMO antenna suppresses surface wave effects, resulting in high isolation among the resonating elements. The EBG unit cell is theoretically examined through its equivalent circuit. The antenna covers the commonly used 26.5–29.5 GHz (n257), 24.25–27.5 GHz (n258), and 27.5–28.35 GHz (n261) 5G mm-wave bands.

REFERENCES

1. Rinne, M. and O. Tirkkonen, "LTE, the radio technology path towards 4G," *Computer Communications*, Vol. 33, No. 16, 1894–906, Oct. 15, 2010.
2. Sharma, D., B. K. Kanaujia, and S. Kumar, "Compact multi-standard planar MIMO antenna for IoT/WLAN/sub-6 GHz/X-band applications," *Wireless Networks*, Vol. 27, 2671–2689, 2021.
3. Zaidi, A. M., M. T. Beg, B. K. Kanaujia, S. Kumar, and K. Srivastava, "A dual-band branch line coupler for LTE 0.7 GHz and LTE 2.6 GHz frequencies," *International Journal of RF and Microwave Computer-Aided Engineering*, Vol. 29, No. 9, e21838, 2019.
4. Khandelwal, M. K., S. Kumar, and B. K. Kanaujia, "Design, modeling and analysis of dual-feed defected ground microstrip patch antenna with wide axial ratio bandwidth," *Journal of Computational Electronics*, Vol. 17, No. 3, 1019–1028, 2018.
5. Lee, G. H., S. Kumar, H. C. Choi, and K. W. Kim, "Wideband high-gain double-sided dielectric lens integrated with a dual-bowtie antenna," *IEEE Antennas and Wireless Propagation Letters*, Vol. 20, No. 3, 293–297, 2021.
6. Pi, Z. and F. Khan, "An introduction to millimeter-wave mobile broadband systems," *IEEE Communications Magazine*, Vol. 49, No. 6, 101–107, Jun. 6, 2011.
7. Qualcomm Technologies, (Dec. 2017), *Spectrum for 4G and 5G*, Accessed: Jan. 5, 2019, [Online], Available: https://www.qualcomm.com/news/media-center.
8. European 5G Observatory, *National 5G Spectrum Assignment*, Accessed: May 10, 2020, [Online], Available: https://5gobservatory.eu/.
9. Rappaport, T. S., S. Sun, R. Mayzus, H. Zhao, Y. Azar, K. Wang, G. N. Wong, J. K. Schulz, M. Samimi, and F. Gutierrez, "Millimeter wave mobile communications for 5G cellular: It will work!," *IEEE Access*, Vol. 1, 335–349, May 10, 2013.
10. Busari, S. A., S. Mumtaz, S. Al-Rubaye, and J. Rodriguez, "5G millimeter-wave mobile broadband: Performance and challenges," *IEEE Communications Magazine*, Vol. 56, No. 6, 137–143, Jun. 18, 2018.
11. Rangan, S., T. S. Rappaport, and E. Erkip, "Millimeter-wave cellular wireless networks: Potentials and challenges," *Proceedings of the IEEE*, Vol. 102, No. 3, 366–385, Feb. 5, 2014.
12. Tiwari, R. N., P. Singh, B. K. Kanaujia, S. Kumar, and S. K. Gupta, "A low profile dual band MIMO antenna for LTE/Bluetooth/Wi-Fi/WLAN applications," *Journal of Electromagnetic Waves and Applications*, Vol. 34, No. 9, 1239–1253, 2020.
13. Kumar, S., G. H. Lee, D. H. Kim, H. C. Choi, and K. W. Kim, "Dual circularly polarized planar four-port MIMO antenna with wide axial-ratio bandwidth," *Sensors*, Vol. 20, No. 19, 5610, 2020.
14. Babu, N. S., A. Q. Ansari, B. K. Kanaujia, G. Singh, and S. Kumar, "Compact two-port ultra-wideband multiple-input-multiple-output antenna with an electromagnetic band gap structure," *Materials Today: Proceedings*, Mar. 27, 2023.
15. Srivastava, K., S. Kumar, B. K. Kanaujia, S. Dwari, H. C. Choi, and K. W. Kim, "Compact eight-port MIMO/diversity antenna with band rejection characteristics," *International Journal of RF and Microwave Computer-Aided Engineering*, Vol. 30, No. 5, e22170, 2020.

16. Khalid, M., S. Iffat Naqvi, N. Hussain, M. Rahman, S. S. Mirjavadi, M. J. Khan, and Y. Amin, "4-Port MIMO antenna with defected ground structure for 5G millimeter wave applications," *Electronics*, Vol. 9, No. 1, 71, Jan. 1, 2020.
17. Gupta, S., Z. Briqech, A. R. Sebak, and T. A. Denidni, "Mutual-coupling reduction using metasurface corrugations for 28 GHz MIMO applications," *IEEE Antennas and Wireless Propagation Letters*, Vol. 16, 2763–2766, Aug. 25, 2017.
18. Zhang, Y., J. Y. Deng, M. J. Li, D. Sun, and L. X. Guo, "A MIMO dielectric resonator antenna with improved isolation for 5G mm-wave applications," *IEEE Antennas and Wireless Propagation Letters*, Vol. 18, No. 4, 747–751, Feb. 27, 2019.
19. Tariq, S., S. I. Naqvi, N. Hussain, and Y. Amin, "A metasurface-based MIMO antenna for 5G millimeter-wave applications," *IEEE Access*, Vol. 9, 51805–51817, Mar. 29, 2021.
20. Elabd, R. H., H. H. Abdullah, and M. Abdelazim, "Compact highly directive MIMO vivaldi antenna for 5G millimeter-wave base station," *Journal of Infrared, Millimeter, and Terahertz Waves*, Vol. 42, 173–194, Feb. 2021.
21. Murthy, N., "Improved isolation metamaterial inspired mm-Wave MIMO dielectric resonator antenna for 5G application," *Progress In Electromagnetics Research C*, Vol. 100, 247–261, 2020.
22. Akbari, M., H. A. Ghalyon, M. Farahani, A. R. Sebak, and T. A. Denidni, "Spatially decoupling of CP antennas based on FSS for 30-GHz MIMO systems," *IEEE Access*, Vol. 5, 6527–6537, Apr. 18, 2017.
23. Farahani, M., J. Pourahmadazar, M. Akbari, M. Nedil, A. R. Sebak, and T. A. Denidni, "Mutual coupling reduction in millimeter-wave MIMO antenna array using a metamaterial polarization-rotator wall," *IEEE Antennas and Wireless Propagation Letters*, Vol. 16, 2324–2327, Jun. 20, 2017.
24. Iqbal, A., A. Basir, A. Smida, N. K. Mallat, I. Elfergani, J. Rodriguez, and S. Kim, "Electromagnetic bandgap backed millimeter-wave MIMO antenna for wearable applications," *IEEE Access*, Vol. 7, 111135–111144, Aug. 8, 2019.
25. Hussain, N., M. J. Jeong, A. Abbas, and N. Kim, "Metasurface-based single-layer wideband circularly polarized MIMO antenna for 5G millimeter-wave systems," *IEEE Access*, Vol. 8, 130293–130304, Jul. 15, 2020.
26. Sharawi, M. S., S. K. Podilchak, M. T. Hussain, and Y. M. Antar, "Dielectric resonator based MIMO antenna system enabling millimetre-wave mobile devices," *IET Microwaves, Antennas & Propagation*, Vol. 11, No. 2, 287–293, Jan. 2017.
27. Hussain, N., M. J. Jeong, J. Park, and N. A. Kim, "A broadband circularly polarized fabry-perot resonant antenna using a single-layered PRS for 5G MIMO applications," *IEEE Access*, Vol. 7, 42897–42907, Apr. 2, 2019.
28. Abo El-Hassan, M., K. F. Hussein, and K. H. Awadalla, "Microstrip antenna with L-shaped slots for circularly polarised satellite applications," *The Journal of Engineering*, Vol. 2019, No. 12, 8428–8431, Dec. 2019.
29. Qian, Y., R. Coccioli, D. Sievenpiper, V. Radisic, E. Yablonovitch, and T. Itoh, "A microstrip patch antenna using novel photonic band-gap structures," *Microwave Journal*, Vol. 42, No. 1, 66–72, Jan. 1, 1999.
30. Yang, F. and Y. Rahmat-Samii, "Microstrip antennas integrated with electromagnetic band-gap (EBG) structures: A low mutual coupling design for array applications," *IEEE Transactions on Antennas and Propagation*, Vol. 51, No. 10, 2936–2946, Oct. 14, 2003.
31. Kumar, A., J. Mohan, and H. Gupta, "Surface wave suppression of microstrip antenna using different EBG designs," *2015 International Conference on Signal Processing and Communication (ICSC)*, 355–359, IEEE, Mar. 16, 2015.
32. Sievenpiper, D., L. Zhang, R. F. Broas, N. G. Alexopolous, and E. Yablonovitch, "High-impedance electromagnetic surfaces with a forbidden frequency band," *IEEE Transactions on Microwave Theory and Techniques*, Vol. 47, No. 11, 2059–2074, Nov. 1999.

33. Yang, F. and Y. R. Sami, "The effects of an electromagnetic bandgap (EBG) structure on two element microstrip patch antenna array," *IEEE Transactions Antennas and Propagation*, Vol. 51, No. 10, 2936–2946, Oct. 2003.
34. Abdulhameed, M. K., M. M. Isa, Z. Zakaria, M. K. Mohsin, and M. L. Attiah, "Mushroom-like EBG to improve patch antenna performance for C-band satellite application," *International Journal of Electrical and Computer Engineering*, Vol. 8, No. 5, 3875, Oct. 1, 2018.
35. Yang, F. and Y. Rahmat-Samii, "Reflection phase characterizations of the EBG ground plane for low profile wire antenna applications," *IEEE Transactions on Antennas and Propagation*, Vol. 51, No. 10, 2691–2703, Oct. 14, 2003.
36. Al-Dulaimi, Z., T. A. Elwi, and D. C. Atilla, "Design of a meander line monopole antenna array based hilbert-shaped reject band structure for MIMO applications," *IETE Journal of Research*, Vol. 68, No. 4, 2353–2362, Jul. 4, 2022.
37. Blanch, S., J. Romeu, and I. Corbella, "Exact representation of antenna system diversity performance from input parameter description," *Electronics Letters*, Vol. 39, No. 9, 705–707, May 1, 2003.
38. Sharawi, M. S., "Printed multi-band MIMO antenna systems and their performance metrics [wireless corner]," *IEEE Antennas and Propagation Magazine*, Vol. 55, No. 5, 218–232, Oct. 2013.
39. Chae, S. H., S. K. Oh, and S. O. Park, "Analysis of mutual coupling, correlations, and TARC in WiBro MIMO array antenna," *IEEE Antennas and Wireless Propagation Letters*, Vol. 6, 122–125, Apr. 10, 2007.
40. De Cos Gómez, M. E., H. Fernández Álvarez, and F. Las-Heras Andrés, "PP-based 24 GHz wearable antenna," *Wireless Networks*, 1–6, Oct. 16, 2023.